



RESEARCH

# Experimental analysis of the extension to shear fracture transition in a rock analogue material using digital image correlation method

Huyen Thi Phuong Tran · Hung Sy Nguyen · Stéphane Bouissou

Received: 10 September 2022 / Accepted: 27 July 2023 / Published online: 9 August 2023  
© The Author(s), under exclusive licence to Springer Nature B.V. 2023

**Abstract** This paper presents the results of axisymmetric extension tests on a Rock Analogue Material that showed a continuous transition from extension fracture to shear fracture with an increase in compressive stress. The analysis used non destructive full-field experimental methods—digital image correlation (DIC), as well as the post-mortem specimens observation. When the mean stress was small, the fractures formed through the mode I cracking at tensile equal to the material tensile strength with smooth surfaces. These surfaces became rougher or delicate plumose patterns as the mean stress increased. Fracture angles also increased progressively from extension fractures to shear fractures. Hybrid fractures formed under mixed tensile and compressive stress states and presented plumose patterns on the rupture surface. DIC results showed the localisation of tensile deformation and the acceleration of deformation at the zone that induced the fracture. The fracture caused a reduction of deformation in the surrounding areas, which showed a release

of elastic energy stored in the material during the propagation of fracture.

**Keywords** Extension test · Hybrid fracture · Plumose · Transition of extension–shear fracture · Digital image correlation

## List of Symbols

$\sigma_1, \sigma_2, \sigma_3$	Principal stress
$\sigma_m$	Mean stress
$q = \sigma_1 - P_c$	Deviatoric stress
$P_c$	Confining pressure
$\Psi$	Angle between fracture/band and $\sigma_1$ direction
$E$	Young's modulus
$\nu$	Poisson's ratio
$\rho$	Density
$\varepsilon_{ax}$	Axial strain
$\tilde{\varepsilon}_{ax}$	Nominal axial strain
$\varepsilon$	Volumetric strain
$\sigma_{ax}$	Axial stress
$\sigma_{ax}^c$	Axial stress at central section of dog-bone sample
$\sigma_{ax}^{ex}$	Axial stress at extremity of dog-bone sample
$\sigma_{ax}^{rup}$	Axial stress at failure
$\sigma_{ax}^{pk}$	Axial peak stress
$\sigma_t$	Uniaxial tensile strength

H. T. P. Tran (✉)  
The University of Danang - University of Technology and Education, 48 Cao Thang street, Da Nang City, Vietnam  
e-mail: tphuyen@ute.udn.vn

H. S. Nguyen  
HCMC University of Technology and Education, Ho Chi Minh City, Vietnam

S. Bouissou  
ESPACE Laboratory UMR 7300, Université Côte d'Azur, 06200 Nice, France

$S_c$	Area at central section of dog-bone sample
$S_{ex}$	Area at extremity of dog-bone sample
$S_{rup}$	Area of the fracture surface
$F_{ax}$	Applied force on the sample
GRAM1	Granular Rock Analogue Material 1
$\beta$	Dilatancy factor
DIC	Digital image correlation
C	Correlation coefficient
$X_i, x_i = \phi_0(X_i)$	Coordinates (in pixels) of homologous points in the reference and deformed images
$\phi_0$	Transformation function

## 1 Introduction

Extension fractures (opening mode) and shear fractures are two basic types of brittle fractures commonly observed in rock deformation experiments. In the laboratory, a shear fracture is produced under a compressive stress state. The fracture surface forms an angle of about  $20^0 - 40^0$  to the maximum principal compressive stress direction  $\sigma_1$ . An extension fracture forms under a tensile stress state, presents an opening mode displacement normal to the fracture surface, which is perpendicular to the minimum principal compressive stress (Jaeger and Cook 1979; Paterson and Wong 2005). Transitional fractures known as hybrid fracture that display both opening and shear mode, are commonly formed under mixed tensile and compressive stress states (Ferrill et al. 2012; Engelder 1999; Ramsey and Chester 2004).

Within the compressive stress regime, the Mohr–Coulomb failure criterion is widely used to predict the brittle failure strength and orientation of shear fractures. As implied by Mohr’s hypothesis, the orientation of the fracture surface is inclined to  $\sigma_1$  at a fracture angle  $\Psi$ , equal to  $\pi/4 \pm \phi/2$ , where  $\tan \phi$  is the slope of the failure envelope in Mohr space (Handin 1969). The failure envelope is generally described as a continuous function from a compressive to a tensile stress state. The Griffith and modified-Griffith criteria predict parabolic failure envelope for mixed tensile and compressive stress states that includes uniaxial tensile failure. The combination of Griffith and Mohr–Coulomb criteria for compressive stress state forms composite

failure envelope that shows the existence of hybrid fractures in the transition from extension to shear fracture (Brace 1960). However, little laboratory work has investigated and demonstrated clearly hybrid fracture formation.

To build up of the adequate theory of inelastic deformation and fracturing/failure of geomaterials requires large sets of good quality experimental data. The majority of the experimental tests of rock samples were performed under axisymmetric compression. There are few data from axisymmetric extension tests and mostly corresponding to the brittle faulting regime. Heard (Heard 1960) performed series of triaxial compression and extension experiments under different conditions. His data shows that the transition under extension occurs at a mean stress  $\sigma_m$  two times greater than under compression. However, the results by Heard do not mention in detail hybrid fractures.

Ramsey and Chester (2004) carried out series of triaxial extension tests with notch-cut samples of Carrara Marble to study the extension to shear fracture transition. Their results demonstrates a continuous transition from extension fracture to shear fracture with an increase in compressive stress. The fracture angle increases with increasing confining pressure corresponding to a change in morphology. The same observation of mechanical behavior and morphological characteristics of fracture surface in extension–shear fracture transition is documented in a study of Bobich (2005) in Berea sandstone. The degree to which these results apply to granular material is uncertain because of distinct differences in rock microstructure.

The documents of hybrid fractures in field are rare. Hybrid fracture is likely an indicator of a tensile minimum effective stress and low differential stress at failure (Ferrill et al. 2012). The surface morphology of hybrid fracture is consistent with the step-tread geometry that indicates fracture formation process through linkage of an array of en echelon, interacting, extension cracks (Engelder 1999; Reches and Lockner 1994). However, the correlation between the microscopic fracture mechanism, macroscopic fracture form and tension–shear strength is still not well understood.

In this study, we investigate brittle failure in a rock analogue (granular, frictional, dilatant and cohesive) material GRAM1 using triaxial extension tests of dog-bone shape samples to verify the existence of hybrid fractures. Based on the previous study by Nguyen et al.

(2011) conducted on the same material, we herein made modifications to the sample geometry and jacket design to improve reproducibility. New pressure cell with transparent windows allows a direct observation of the sample surface during loading. We therefore can apply the Digital image correlation technique (DIC), one of the most widespread full-field measurement techniques (Viggiani and Hall 2008; Dautriat et al. 2011; Bésuelle and Lanatà 2016; Tran et al. 2019) to obtain the displacement field and calculate the strains during the sample deformation. One of the main advantages of DIC is the non-contact optical application, which reduces the samples' interaction, preserving the best sample state at different deformation stages (Pan et al. 2009). Measuring displacements and strains in real time is carried out by comparing pairs of digital images at the first stage (or undeformed stage) and the deformed stage through a mathematical correlation analysis. Various studies have shown that the 2D DIC technique is suitable when applied to fracture case studies (Lin et al. 2019; Bertelsen 2019; Nguyen et al. 2017) and it offers high accuracy and reduced computational complexity compared with other techniques such as analytical method, and finite element method (Bermudo Gamboa et al. 2019).

For 3D objects and to avoid limiting the study to planar specimens and no-out-of plane motion, 3D DIC technique can be well applied (Chen et al. 2018; Molina-Viedma et al. 2018). The number of cameras has to be increased and positioned to take images from different angles. The 3D DIC needs a proper calibration of the axis before placing the samples and starting the tests. For a general analysis of the process, the 2D DIC analysis can be proposed instead of the 3D DIC (Bermudo Gamboa et al. 2019). For instance, Tran et al. (2019) applied the 2D DIC technique to detect the initiation and evolution of a network of deformation bands on cylindrical samples. In this case, the vertical component of displacement is of more interest. Measurement results were shown to be little affected by the curved geometry of sample. The axial strain maps obtained by DIC represented the post-mortem bands pattern faithfully (Tran et al. 2019).

On the basis of the data (the conditions of formation, fractography of fractures, and strain field), we discuss the fracturing mechanism and argue the existence of continuous transition from extension fracture to shear fracture. Hybrid fractures form under mixed tensile and compressive stress states. The surface morphology of

hybrid fracture will be then described in detail. DIC results show the localisation of tensile deformation and an acceleration of deformation at the zone that induces the fracture. The fracture causes the reduction of deformation in the surrounding areas. This shows a release of the elastic energy stored in the material during the propagation of fracture.

## 2 Sample description

### 2.1 Material characterization

The experiments presented in this article were carried out on GRAM1 (Granular Rock Analogue Material 1). Its fabrication procedure and properties were described in detail in the previous studies (Nguyen et al. 2011; Mas and Chemenda 2014, 2015). GRAM1 was made from a finely ground powder of  $\text{TiO}_2$ . The average grain size is  $\sim 0.3 \mu\text{m}$ . The powder was subjected to the hydrostatic pressure of  $P_{fab} = 2\text{MPa}$ , at which the grains were bonded one to another. An extensive program of GRAM1 stress-strain measurements in axisymmetric compression and extension tests at different confining pressure  $P_c$  below  $P_{fab}$  shows that material is quite relevant to the real rocks. It has frictional, cohesive, dilatant properties and mechanical behavior very similar to those of real rocks, but is about 2 orders of magnitude less strong and less rigid than rocks (Fig. 1) (Nguyen et al. 2011).

The Young's modulus  $E$  of GRAM1 is  $6.5 \times 10^8$  Pa, the Poisson's ratio  $\nu$  is 0.25, the internal friction coefficient  $\alpha$  is of  $\sim 0.6$ . Its porosity is about 50% and the density  $\rho$  is  $1723 \text{ kg/m}^3$ . As for real rocks, the dilatancy factor  $\beta$  for GRAM1 is pressure-dependent and reduces from positive to negative values with  $P_c$ . The GRAM1 data reported in Nguyen et al. (2011) showed that the dilatancy factor  $\beta$  for the extension conditions varies from 0.4 (at  $P_c = 0.4 \text{ MPa}$ ) to  $-0.4$  (at  $P_c = 1.5 \text{ MPa}$ ).

### 2.2 Preparation of samples

In extension tests, it is necessary to apply a tensile axial stress  $\sigma_{ax}$  to reach the rupture in the sample. Hoek (1964) and Brace (1964) were able to make the axial stress tensile using dog-bone shaped samples in a triaxial cell, where  $\sigma_1 = \sigma_2 > \sigma_3$ . In practice, both  $\sigma_1$  and  $\sigma_3$

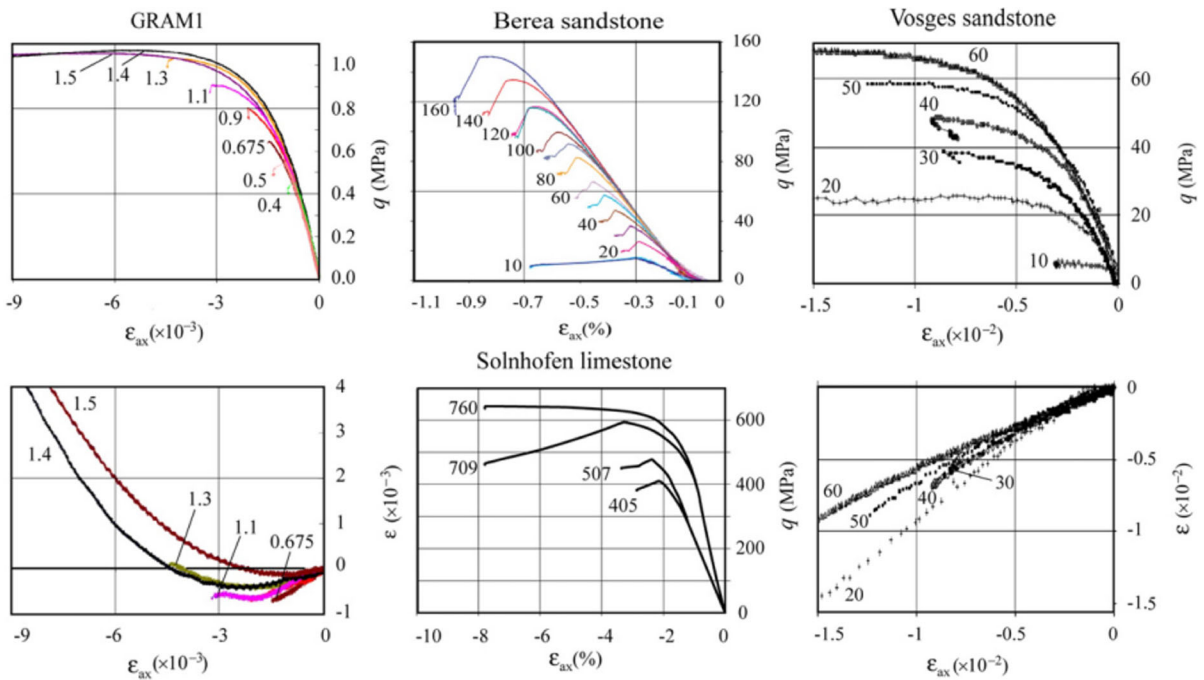


**Fig. 1** Comparison of the curves of deviatoric stress–axial strain  $q(\epsilon_{ax})$  and volumetric strain–axial strain  $\epsilon(\epsilon_{ax})$  for GRAM1 and rocks for extension tests. The plots for the rocks are from: Solnhofen limestone, Vosges sandstone (Nguyen et al. 2011)

are increased to confine the sample.  $\sigma_3$  then applies a pressure on the curved portion of the sample and causes extension. The axial stress is, therefore, decreased to failure (Perras and Diederichs 2014). Two different dog-bone samples are usually used in the extension tests: sample shape with constant-radius segment  $r_{min}$  (Fig. 2a) (Millar and Murray 1988; Bésuelle et al. 2000) and sample shape with constant along-axis curvature of the surface  $R_0$  (Fig. 2b) (Ramsey and Chester 2004; Bobich 2005). In the present work, we used the latter case to insure the fracture forming in the central thinned zone where the sample deformation was recorded during the test. From the images capturing, we applied the DIC technique to obtain the displacement and strain fields during the sample deformation.

The maximal tensile axial stress that can be generated in the thinned section of the dog-bone sample is defined by both confining pressure  $P_c$  and ratio  $r_{max}/r_{min}$  as in Perras and Diederichs (2014); Nguyen (2009):

$$\sigma_{ax}^c = \sigma_{ax}^{ex} S_{ex} - \frac{P_c(S_{ex} - S_c)}{S_c} \tag{1}$$

where,  $\sigma_{ax}^c$  and  $\sigma_{ax}^{ex}$  are axial stresses in central section and at the extremity, respectively;  $S_c$  and  $S_{ex}$  are

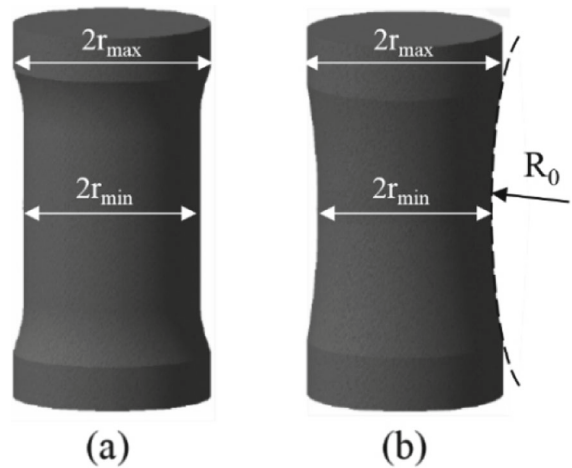
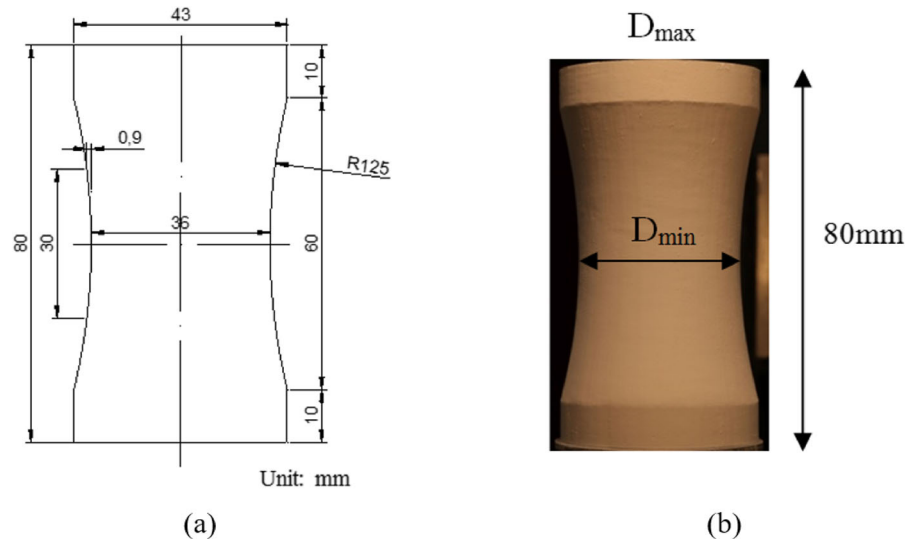


**Fig. 2** Dog-bone shape of GRAM1 samples. Samples with **a** constant-radius segment  $r_{min}$ ; **b** constant along-axis curvature of the surface  $R_0$  (Nguyen et al. 2011)

the areas of the central section and of the extremity, respectively.

Figure 3 presents the dog-bone GRAM1 sample used in extension tests. The smallest and the biggest diameters are about 36 mm and 43 mm, respectively.

**Fig. 3** Dog-bone shape of GRAM1 samples with specific dimensions: **a** design drawings; **b** GRAM1 sample



The sizes of these two diameters are chosen to ensure that the sample wrapping by latex jacket (a thin transparent latex film of about  $300\ \mu\text{m}$  thickness) is convenient and does not affect the image matching procedure. Usage of latex film and specifications of DIC technique will be presented in the following sections.

### 3 Experimental setup and instrumentation

To perform an extension test, we followed the general methodology of previous extension tests on dog-bone shape samples (Ramsey and Chester 2004; Nguyen et al. 2011), but made modifications to the sample geometry and jacket design to improve reproducibility. The upper platen is similar to that used in Nguyen et al. (2011) for extensive tests. This helps reduce the deviation of the sample stress-state from the axial symmetry that can occur during the deformation. The sample and platens were jacketed by a transparent latex film ( $\sim 300\ \mu\text{m}$  of thickness) and placed into a pressure cell of 2 MPa capacity filled with clean water. The water pressure  $P_c$  was increased to the studied value by a 3 MPa capacity-pressure generator. The sample was then unloaded in the axial direction at  $P = \text{const}$  by the piston moving with a velocity of  $10^{-6}$  m/s. During this process, stresses were measured by an internal force sensor with a frequency of five measurements per second. Due to the small thickness and rigidity, the latex

film can follow exactly the displacement of the sample surface (Tran et al. 2019). For DIC analysis, a speckle-like pattern was sprayed on the transparent latex film to provide the surface with characteristic features. The droplets should be of an almost uniform size (of a few pixels, in our case about of 3-10 pixels), and sufficient density. The latter helps to increase the accuracy of DIC measurements (Dautriat et al. 2011; Tran et al. 2019).

To obtain the displacements, we applied the 2D digital image correlation technique. As shown in the Fig. 4, two high resolution cameras ( $2752 \times 2204$  pixels) are mounted on fixed frame on two sides of plane windows of the pressure cell to ensure a fully stable position. It is important to align the axes of the cameras perpendicularly to these plane windows and keep a diffuse, homogeneous and unchanging illumination during the exposure time. During loading, images covering on the whole sample height were taken simultaneously at a frequency of 10 Hz. The digital correlation of the images taken by these two cameras is then performed to obtain displacement fields, strain fields and their evolution.

After the test, the sample was unloaded in a way not to cause additional inelastic deformation: the axial nominal stress was first increased to  $P_c$ , after which the complete unloading followed a hydrostatic path.



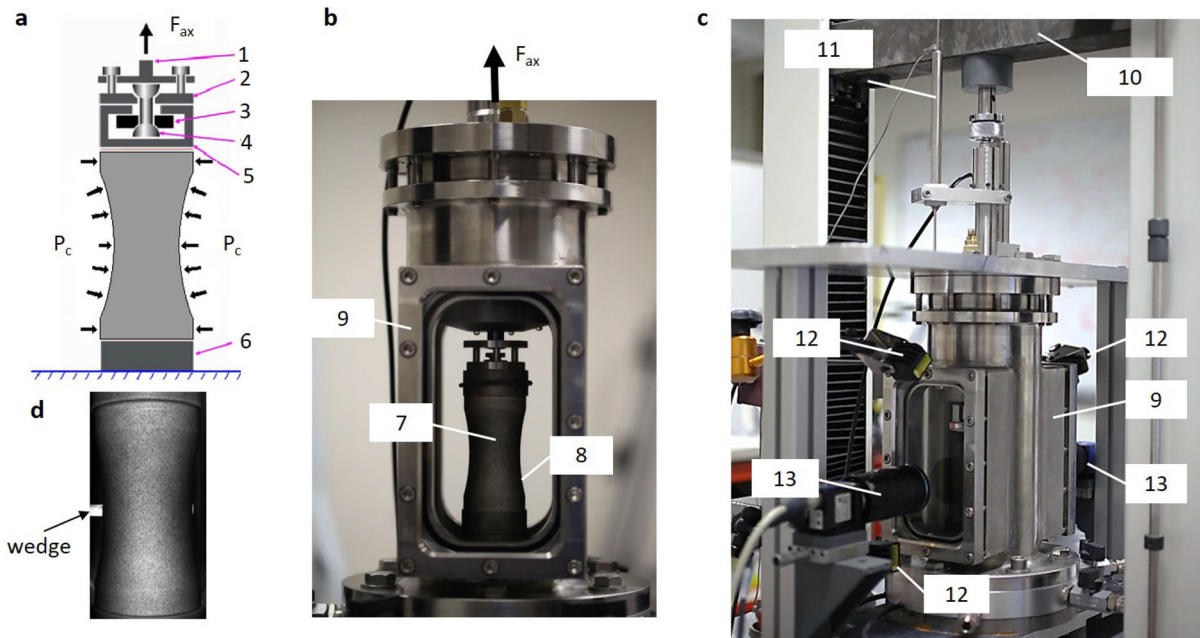


**Fig. 4** Scheme of sample and the platens designed for the extension test (a), photo of the pressure cell with the GRAM1 sample (b), photo of the experimental setup (c) and photo of a GRAM1 sample with a wedge glued in the central part; the sample and platens were jacketed by a latex film with speckle-like pattern

(d). (1) hook, (2) connector, (3) sliding piece, (4) rod with two ball joints, (5) hull, (6) lower platen, (7) dog-bone-shape sample, (8) latex film with speckle-like pattern, (9) pressure cell, (10) press cross, (11) external displacement sensor, (12) LEDs, (13) cameras

## 4 Methods of obtaining data

### 4.1 Post-mortem sample observation

After removing the sample from the pressure cell, the orientation of the fractures/deformation bands was determined thanks to traces appearing on the jacket. Fracture orientation can be either measured from the trace on the latex jacket or from the photos taken perpendicularly the surface of the post-mortem sample. Fracture orientation was identified by the maximum angle between the fracture surface and the plane normal to the cylinder axis. Similar observations were made by [Bésuelle et al. \(2000\)](#) and [Nguyen \(2009\)](#). The lines described as “white, chalky zones” on the latex jacket were identified as the trace of bands or failure surfaces.

The fractures, occurring in the extension test, correspond to very thin discontinuities on the surface of the sample. The fracture surfaces after opening these discontinuities exhibit a feathery topography, known as “plumose pattern”, characterized by ridges and valleys forming a divergent pattern. The observation of the

plumose patterns generated in the series of extension tests will be considered carefully and documented in the session following.

### 4.2 Digital image correlation technique

The DIC technique has been widely used in studying the mechanical response of different materials such as metals, ceramics, rocks and rock analogue ([Viggiani and Hall 2008](#); [Dautriat et al. 2011](#); [Bésuelle and Lanatà 2016](#); [Tran et al. 2019](#)) thanks to its advantages as a measurement method without contact with the observed sample. Numerous DIC softwares have been developed. In this work, we use software “7D” which was used and described in our previous study ([Tran et al. 2019](#)).

The DIC software 7D was developed at the Applied Mechanics Laboratory in Annecy by [Vacher et al. \(1999\)](#). It supports most common formats of images (.tif,.jpeg,.bmp,.emf...), coded on 8 or 12 bit, black and white or colour. After determining a reference image and one or a set of images to correlate, the

user defines a grid in the analyzed area on the reference image and images at different deformation stages. Around each grid node, a square correlation window size, known as subset size, is then defined. The subset sizes are between 6 and 40 pixels. A too small subset is likely to give false correlations due to an increase in the number of local minimum on the surface of the correlation coefficients. However, larger subset also leads to the increase of computational time (Perras and Diederichs 2014). The DIC parameters used in our analyses are: the subset (correlation window) of  $10 \times 10$  pixels (corresponding to an area of  $0.32 \times 0.32$  mm) and the step (grid spacing) of 10 pixels. The DIC algorithm is designed to find the most similar pixel subsets corresponding to the correlation window in the reference image and images at respective different deformed stages by optimizing a correlation coefficient defined as (Tran et al. 2019; Vacher et al. 1999):

$$C = 1 - \frac{\sum_{i \in D} f(X_i) - \bar{f} \times (g(x_i) - \bar{g})}{\sqrt{\sum_{i \in D} (f(X_i) - \bar{f})^2 \times \sum_{i \in D} (g(x_i) - \bar{g})^2}} \tag{2}$$

where,  $D$  is the correlation window area.  $X_i$  and  $x_i = \phi_0(X_i)$  are respectively the coordinates (in pixels) of homologous points in the reference and deformed images.  $\phi_0$  is the transformation function.  $f(X_i)$  and  $g(x_i)$  are respectively the grey levels of point  $i$  in the reference and deformed images;  $\bar{f}$  and  $\bar{g}$  are respectively the averages of the grey levels in the correlation window in the reference and deformed images.

The coefficient  $C$  ranges from 0 to 1.  $C$  tends to zero when images have a perfect similarity, whereas  $C$  equals one corresponding to no match at all. The position of the deformed correlation window is determined as the correlation coefficient  $C$  reaches the minimum value. The software “7D” computes the difference in the positions of grid nodes in the reference and deformed images, and yields a displacement field based on two assumptions: (1) the displacement field is continuous and (2) initially square correlation windows are transformed into any quadrilateral zones during the deformation. The analysis of the displacement of four points assumes a bilinear displacement field  $U$  of the type  $U = ax + by + cxy + d$ , where  $a$ ,  $b$ ,  $c$ , and  $d$  are the coefficients computed at each deformation stage. The strain field is then calculated using large strain Green Lagrange formulation. The precision obtained on the displacement field can reach 0.01 pixel. This precision

makes it possible to calculate the strains in a large range, from elastic strains ( $\pm 0.01$  percent) to large strains (over 200 percent) (Vacher et al. 1999).

*Axial deformation measurement.* The dog-bone shaped sample causes a difficulty in ensuring a good depth of field on the entire surface of the sample, especially on the transitional areas between the central part and the extremity. This can decrease the accuracy of the strain measurement performed by the DIC technique. As mentioned in the introduction, the curved shape of the sample can lead to the computational limitations when using 2D DIC technique. The vertical component of displacement is therefore chosen to exploit. The axial deformation measurement is focused in the central zone where the fracture exists. This can reduce the impact of the curved shape on the results.

Figure 5c and d present the accumulated axial strain map at the early stage of the representative test E0.8-10T and the deformations in the central profile along the height of the sample. Those maps show that the material in the central part of about 30 mm in height is performed quasi-homogeneously. Note that, the latex film jacketed the sample deforms following the deformation of the material during loading. At the moment of rupture, it can be pressed into the space produced during the opening of the fracture and thus induces a very large value of deformation in the heart of the fractured zone (Fig. 6c) and a very thick fracture as shown by DIC (Fig. 6b). In order to better represent the differential stress–strain curve  $q(\tilde{\epsilon}_{ax})$ , the nominal axial strain  $\tilde{\epsilon}_{ax}$  is thus calculated in this central zone of 30 mm in height (two red squares of  $30 \times 30$  pixels) (Fig. 6).

## 5 Results and discussion

A total of 40 extension tests have been conducted at the confining pressure  $P_c$  from 0.25 to 0.9 MPa. This  $P_c$  range is decided from the previous study of Nguyen et al. (2011). The aim is to focus on the transition  $P_c$  from the extension to shear fracture. At the confining pressure  $P_c$  ranging from 0.7 to 0.8 MPa, two experimental cases are performed: normal tests (without using wedge) and tests with a wedge glued to the central of the sample. The usage of wedge is to study the influence of a prechosen point on the initiation and evolution of a deformation band/fracture. The results

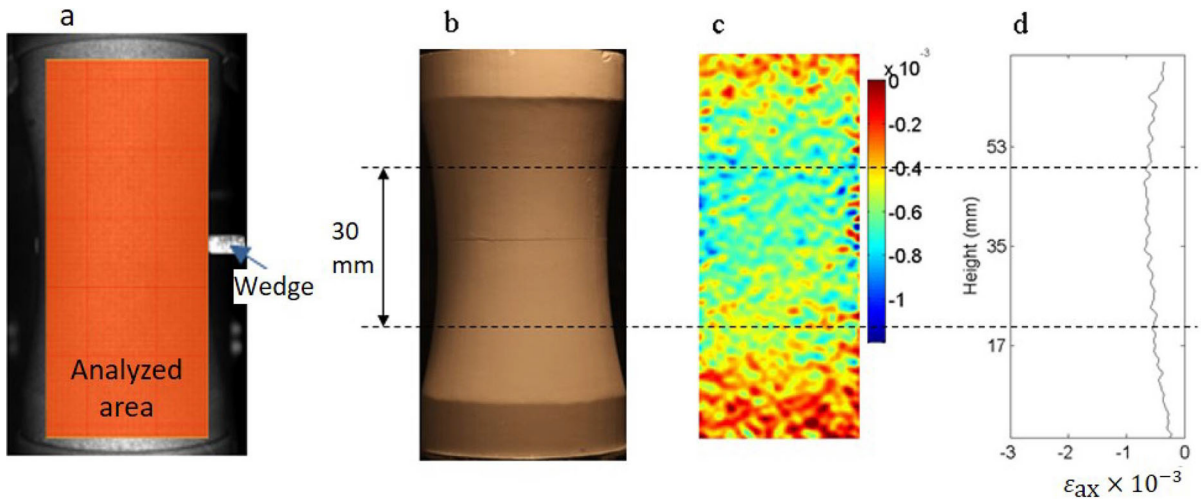
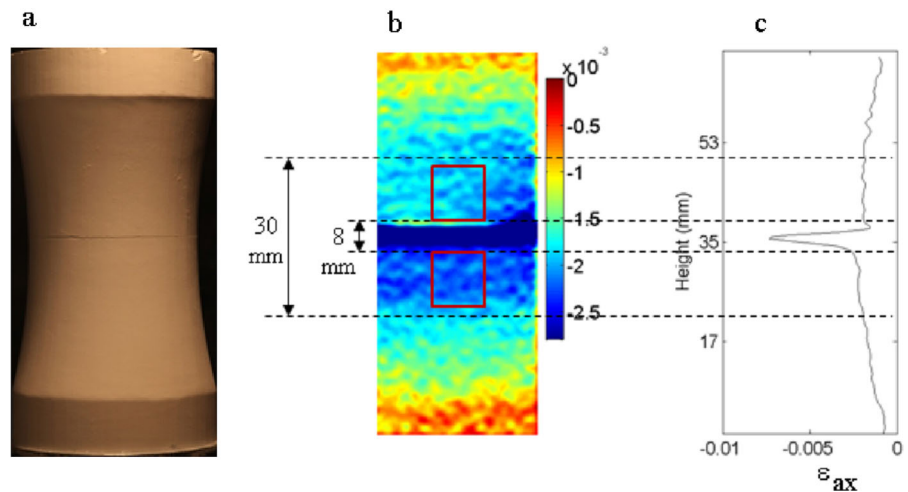


**Fig. 5** E0.8-10T test. **a** An example of an image recorded during the test with the resolution 1 pixel  $\sim 31.2 \mu\text{m}$ , analyzed area in yellow, analysis grid in red; **b** post-mortem sample; **c** axial strain

map ( $\epsilon_{ax}$ ) at the early deformation stage; **d** deformations at the central profile along the height of the sample

**Fig. 6** E0.8-10T test. **a** Post-mortem sample; **b** axial strain map ( $\epsilon_{ax}$ ) corresponding to the moment of failure; **c** axial strain map at the central profile along the height of the sample. The thickness of the fractured area is about 8 mm. The two red squares of  $30 \times 30$  pixels are used to calculate the nominal axial deformation



of 22 representative experiments are presented in the Table 1.

The axial stress at failure  $\sigma_{ax}^{rup}$  (or axial peak stress  $\sigma_{ax}^{pk}$ ) is calculated by dividing the applied force by the rupture area (Perras and Diederichs 2014):

$$\sigma_{ax}^{rup} = \sigma_3^{rup} = P_c - \frac{F_{ax}}{S_{rup}} \tag{3}$$

where,  $P_c$  is the confining pressure;  $F_{ax}$  is the applied force on the sample;  $S_{rup}$  is the the area of the horizontal section of the sample at rupture.

As shown in Table 1, an axial tensile stress is obtained at rupture in all the tests carried out at con-

fining pressures  $P_c$  below 0.8 MPa. At  $P_c$  less than 0.5 MPa,  $\sigma_{ax} = \sigma_3$  decreases (becomes more extensive) by  $-0.071$  (cf. Fig. 7, close to the uniaxial tensile strength of GRAM1  $\sigma_t = -0.07$  MPa (Ferrill et al. 2012) to  $-0.13$  MPa with increasing  $P_c$ .  $\sigma_3$  increases (becomes more compressive) as a function of  $P_c$  when  $P_c \geq 0.5$  MPa. At  $P_c = 0.8$  MPa, the axial stress at rupture  $\sigma_{ax}^{pk} = \sigma_3^{pk}$  is very close to 0.



**Table 1** Results of GRAM1 triaxial extension experiments

Test	$P_c = \sigma_1$	Axial peak stress $\sigma_{ax}^{pk}$	$\Psi$ (°)
E0.25-01T <sup>a</sup>	0.25	-0.071	0
E0.25-02T <sup>a</sup>	0.25	-0.106	0
E0.3-04T <sup>a</sup>	0.3	-0.101	0
E0.3-06T <sup>a</sup>	0.3	-0.120	0
E0.35-04T <sup>a</sup>	0.35	-0.130	0
E0.4-01T <sup>a</sup>	0.4	-0.099	0
E0.4-02T <sup>a</sup>	0.4	-0.129	0
E0.5-01T <sup>a</sup>	0.5	-0.130	0
E0.5-02T <sup>a</sup>	0.5	-0.112	0
E0.5-05T <sup>a</sup>	0.5	-0.096	0
E0.6-02T <sup>a</sup>	0.6	-0.114	0
E0.6-03T <sup>a</sup>	0.6	-0.087	0
E0.7-03T <sup>a</sup>	0.7	-0.047	0
E0.7-01T <sup>a</sup>	0.7	-0.030	1
E0.7-02T <sup>a</sup>	0.7	-0.020	3.8
E0.7-04T <sup>a</sup>	0.7	-0.059	1
E0.7-05T <sup>b</sup>	0.7	-0.019	1
E0.7-06T <sup>b</sup>	0.7	-0.020	1
E0.8-06T <sup>a</sup>	0.8	-0.0064	12
E0.8-08T <sup>a</sup>	0.8	-0.0059	13
E0.8-09T <sup>a</sup>	0.8	-0.0076	13
E0.8-10T <sup>b</sup>	0.8	-0.0066	1
E0.8-11T <sup>b</sup>	0.8	-0.0097	1
E0.9-02T <sup>a</sup>	0.9	0.024	17

$\sigma_{ax}^{pk}$  is the axial peak stress;  $\Psi$  is the angle between the fracture/band and the  $\sigma_1$  direction. In the name of tests, E0.25-01T for example, E stands for extension test, 0.25 is the value of confining pressure at which the test was conducted, 01 is the test order, and T stands for the author's name

<sup>a</sup> Normal tests (without wedge)

<sup>b</sup> Tests with one or more wedges glued to the center of the sample

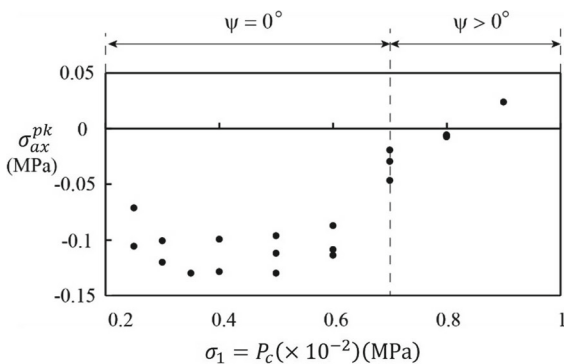


**Fig. 7** Axial stresses at rupture  $\sigma_{ax}^{pk} = \sigma_3^{pk}$  versus the confining pressure  $P_c$

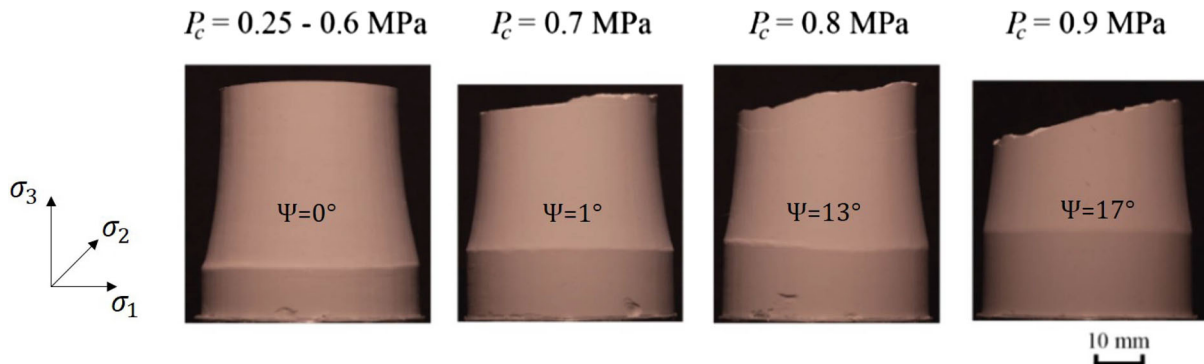
### 5.1 Fracture characteristics

Figure 8 presents the photos of the post-mortem half samples in the extension tests at different  $P_c$ . The angle  $\Psi$  between the fractures and the direction of the principal stress  $\sigma_1$  strongly depends on  $P_c$  or the mean stress  $\sigma_m$  (for extension tests,  $(\sigma_1 + \sigma_2 + \sigma_3)/3 = (2 \times P_c + \sigma_{ax})/3$ , where  $\sigma_1 = \sigma_2 = P_c$ ,  $\sigma_3 = \sigma_{ax}$ ). At  $P_c < 0.7$  MPa ( $\sigma_m < 0.47$  MPa), the fractures are perpendicular to the direction of the axial stress. Their formation is accompanied by acoustic emission (audible noise) which proves the dynamic brittle failure of the material. At  $P_c = 0.7$  MPa, the fracture is either horizontal or inclined with a low  $\Psi < 4^\circ$ . For  $P_c > 0.8$  MPa, several oblique bands are formed in the central zone of the sample (Fig. 10a).

The evolution of the fracture angle as a function of  $P_c$  is shown on the graph ( $\Psi, P_c$ ) in Fig. 9. The fracture angles  $\Psi$  formed at  $P_c < 0.7$  MPa are equal to  $0^\circ$  and are therefore independent of the confining pressure  $P_c$ . From  $P_c \geq 0.7$  MPa,  $\Psi$  increases almost linearly with  $P_c$ . However, we can see that the tests with a wedge glued to the center of the sample at  $P_c = 0.8$  MPa, present a quasi-horizontal fracture ( $\Psi < 1^\circ$ ) (the tests E0.8-10T, E0.8-11T) whereas for the tests without wedge the angle of fractures is about  $13^\circ$  (Table 1). In the case of  $P_c = 0.7$  MPa, the wedge also has a similar influence on the angle of fracture. This can be explained by the concentration of pressure thanks to the wedge that guides the fracture to form and propagate on a plane.

Figures 10 and Fig. 11 show the fracture surfaces after separating manually the samples generated at different confining pressures  $P_c$ . The surfaces of fractures exhibit faint and delicate ridges and troughs forming a plumose topography complicated with steps appearing at relatively high pressures. At  $P_c = 0.7$  MPa, the plumose topography is complicated with steps (Fig. 11c). For  $P_c \geq 0.8$  MPa, the fracture surface is characterized by sputtered plates or zones (Fig. 11e and f). The location of the plates can connect on both sides of the fracture. Furthermore, we can see clearly the influence of attaching a wedge of the testing sample. The fracture surfaces in the case with a wedge (both  $P_c = 0.7$  MPa and 0.8 MPa) still present a plumose morphology, but with a greater relief in the case of 0.8 MPa confining pressure (Fig. 11d and f).

As shown in Fig. 10, the test E0.8-08T carried out at  $P_c = 0.8$  MPa causes two types of fracture



**Fig. 8** Photos showing fracture angle formed in axisymmetric extension tests at different confining pressure  $P_c$ . The angle  $\Psi$  between the fracture plan and the  $\sigma_1$  direction increases with  $P_c$

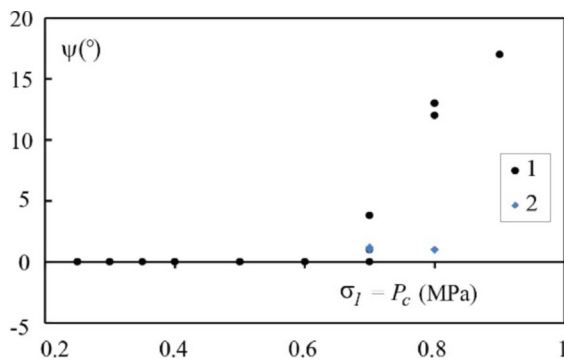


**Fig. 9** Evolution of the fracture angle  $\Psi$  with the confinement pressure  $P_c$  in the extension tests: (1) normal tests (without wedge); (2) tests with one or more wedges glued to the center of the sample

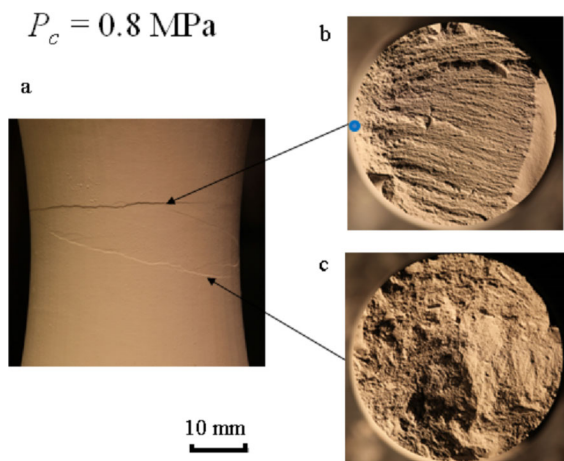


**Fig. 10** Fracture surfaces in the test (normal test, without wedge) at  $P_c = 0.8 \text{ MPa}$  **a** test E0.8-08T which includes, **b** the plumose surface of the weak inclined fracture and **c** the pulverized surface of the oblique fracture. The blue point indicates the fracture initiation point

surfaces. The first one is characterized by sputtered plates or zones as described in the above test E0.8-09T (Fig. 11e). The second one comprises two distinct parts: smooth part and the other manifesting a plumose fractography. The part of this surface with a plumose feature corresponds to the discontinuity seen at the sample surface after unloading, and the smooth part was formed during the manual extension at  $P_c = 0$  due to the fracture propagation from the discontinuity front. This demonstrates a possibility of the formation of mixed horizontal-oblique fractures under a state of mixed tensile and compressive stress.

The series of triaxial extension tests was performed on identique dog-bone shape of GRAM1 samples for different confining pressures  $P_c$ . Extension tests by [Nguyen \(2009\)](#) were also carried out with the GRAM1 material but with two different dog-bone shape samples (Fig. 2). These different shapes may influence the value of the tensile strength as GRAM1 is a low strength analogue rock material. Our results show a continuous transition from extensive fracture to shear fracture with increasing compressive stress. The horizontal (extensive) fractures form for the tests at  $P_c$  from 0.25 to 0.7 MPa under a negative stress state. While at  $P_c$  from 0.7 to 0.9 MPa, shear fractures occur with an increase in fracture angle  $\Psi$  as a function of  $P_c$  under a negative to positive stress state. In addition, the morphology of fracture surfaces show a strong correlation to confining pressure. At  $P_c$  of 0.7 to 0.8 MPa, fractures formed under a mixed tensile and compressive stress state, display both opening and shear mode as hybrid fractures. This is in agreement with the results for the extension tests carried out on real rocks in which the same shape

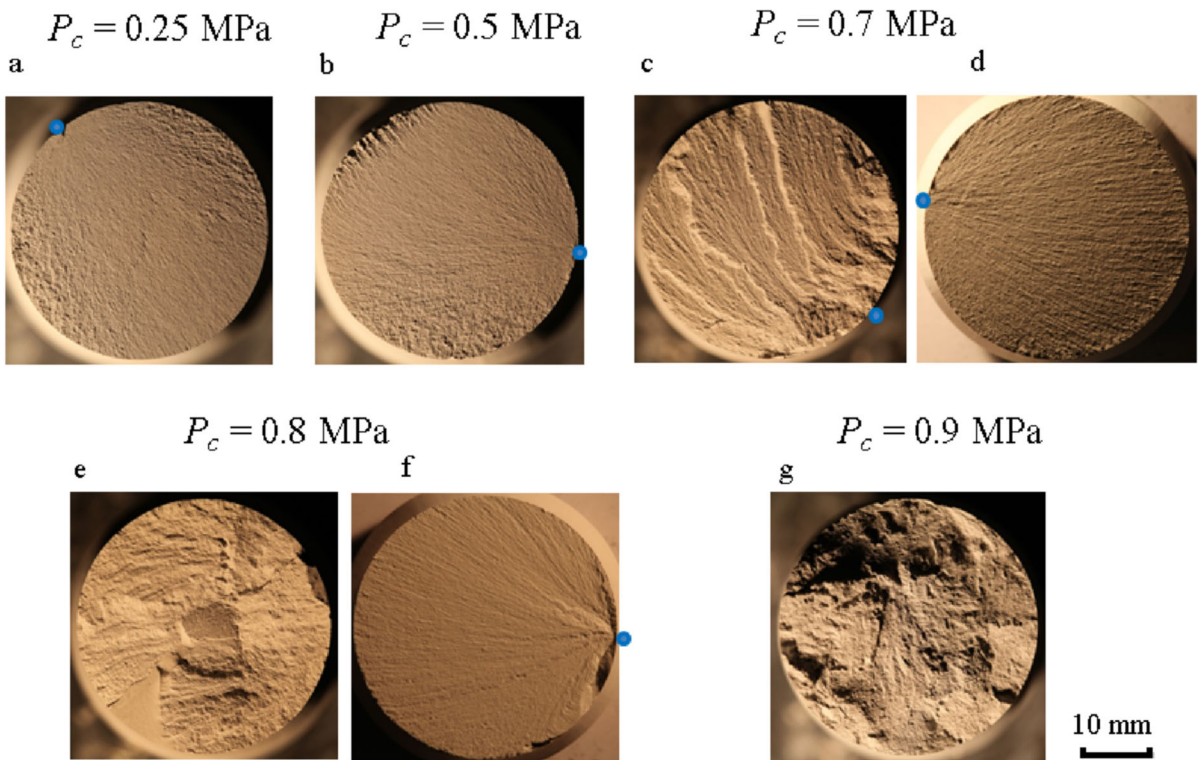


**Fig. 11** Surfaces of orthogonal fractures  $\sigma_3$  generated at different  $P_c$ : **a** test E0.25-02T; **b** test E0.5-02T; **c** test E0.7-02T; **d** test E0.7-06T (with wedge); **e** test E0.8-09T; **f** E0.8-10T (with wedge); **g** test E0.9-02T. The blue point indicates the fracture initiation point

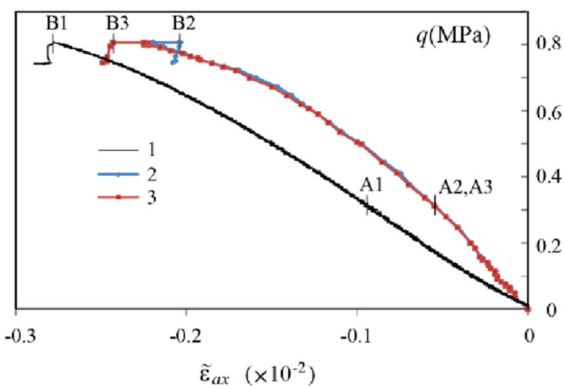


**Fig. 12** Differential stress–strain curves  $q(\tilde{\epsilon}_{ax})$  from test E0.8-10T: 1,  $\tilde{\epsilon}_{ax}$  is calculated from the displacements measured by the external LVDT sensor located between the piston and the pressure cell; 2,  $\tilde{\epsilon}_{ax}$  is the average of the axial DIC strains in the 30 mm height of central zone; 3,  $\tilde{\epsilon}_{ax}$  is the average of the axial DIC strains in the two area of  $30 \times 30$  pixels outside the fracture area. Points A1, A2, A3 are the same points at the same loading stage, points B1, B2, B3 at the moment of rupture

of the sample was used. Ramsey and Chester (2004); Bobich (2005)

### 5.2 Nominal stress–strain curve and deformation evolution during loading

Figure 12 presents the differential stress–strain curves  $q(\tilde{\epsilon}_{ax})$  from the representative test E0.8-10T. The  $q(\tilde{\epsilon}_{ax})$  curve (curve 3, in red) computed by DIC in the two areas of  $30 \times 30$  pixels outside the fracture area as described in the section above, is obviously different from that obtained by the external LVDT sensor (curve 1, in black). The estimated Young’s modulus is  $E \approx 6.5 \times 10^8$  Pa. This value is also close to that determined by the same technique in the compression tests (Tran et al. 2019). However, at the time of failure, this curve shows a stress plateau. This phenomenon can be explained by the impact of the jacket which enters the fracture during its opening. The jacket deforms following the deformation of the material during loading. Upon rupture, the jacket can be pressed into the space produced during the opening of the fracture and also damage the two edges of the fracture. These, therefore, induce a very large value of deformation in the heart of the fractured zone (Fig. 6c) and a very thick fracture

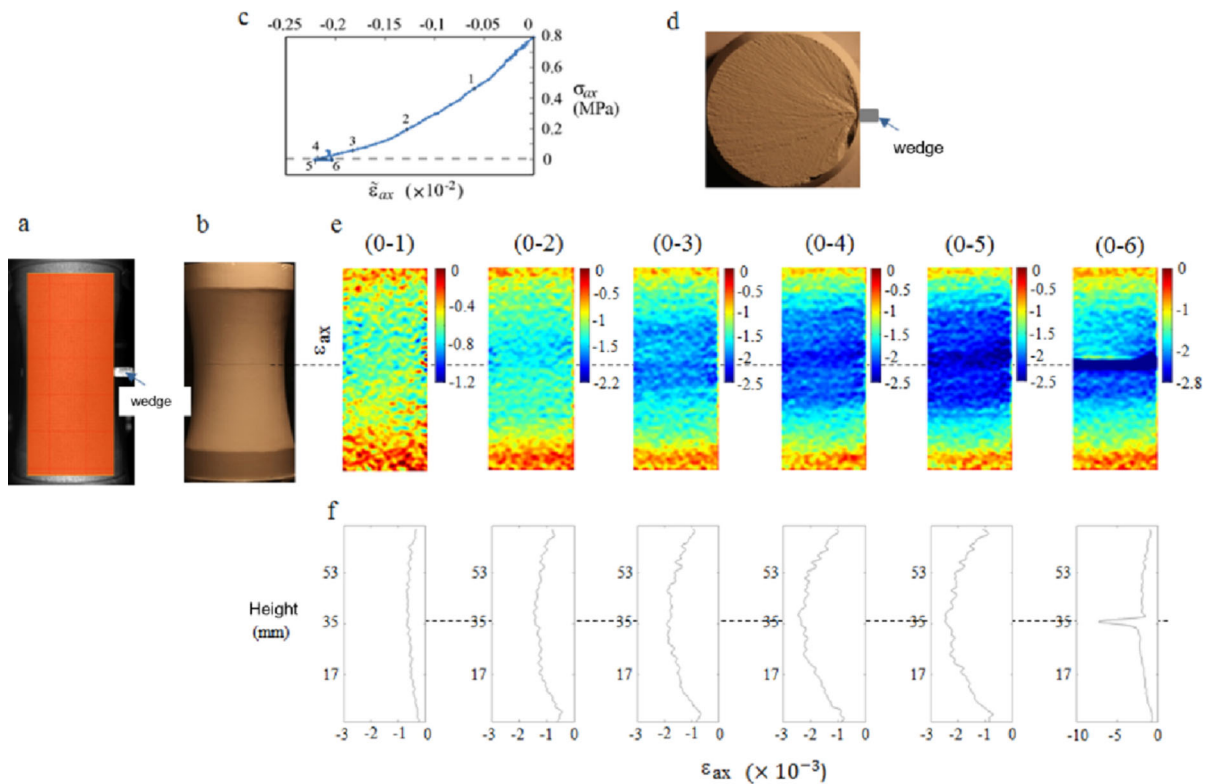


**Fig. 13** Test E0.8-10T: **a** sample set up before testing. The wedge is glued outside the jacket on the right; **b** post-mortem sample with the horizontal fracture; **c** stress–strain curve  $\sigma_{ax}(\tilde{\varepsilon}_{ax})$ ; **d** plumose surface of the fracture. The fracture initiation point coincides with the place of bonding of the wedge; **e**,

**f** Accumulated axial strain maps and strains in the central profile along the height of the sample obtained from DIC between point 0 (at the beginning of test) and points  $n$ , where  $n = 1, 2, \dots, 6$ . The numbers on the color palettes are the strain values multiplied by  $10^{-3}$

as shown by DIC (Fig. 6b). To avoid the existence of the plateau on the curve  $q(\tilde{\varepsilon}_{ax})$ , two square areas of  $30 \times 30$  pixels ( $\approx 9.4 \times 9.4 \text{ mm}^2$ ) above and below the horizontal fracture were chosen to calculate the global deformation. The curve  $q(\tilde{\varepsilon}_{ax})$  obtained by this calculation method (curve 2) (Fig. 12) coincides with the curve obtained previously (curve 3). The return of the strain value at the time of fracture (point B2) shows the release of elastic energy in the material when the fracture occurs.

In extension tests, a horizontal fracture (fracture in opening mode) generally forms under an extensive stress state at low confining pressure  $P_c$ . At higher  $P_c$ , oblique fractures (shear mode) form under a compressive stress state (Ramsey and Chester 2004; Bobich 2005). The extension tests carried out at different confinement pressures from 0.25 to 0.9 MPa show that the type of horizontal fracture can also occur under

the mixed tensile and compressive stress state at  $P_c$  between 0.7 and 0.8 MPa. Therefore, a test at  $P_c = 0.8$  MPa is chosen to present the evolution of the deformation during loading by applying the image correlation technique. A wedge is glued outside the jacket to guide the initiation location and the propagation direction of the fracture.

Figure 13 presents the accumulated axial strain maps for the representative test E0.8-10T. A dotted line indicates the position of the fracture. Significant noise can be seen at the ends of the sample. This can be explained by a shallow depth of field and the dog-bone shape, which gives a blurred effect at the edge of the sample. Therefore, we only analyze the evolution of the deformation in the central zone of about 30 mm height on the  $\varepsilon_{ax}$  maps and the associated  $\varepsilon_{ax}(h)$  graphs. In Fig. 13d, we can see that the sample deforms homogeneously at stage 1, then heterogeneously from stage 2. The  $\varepsilon_{ax}$



maps at stages 3, 4, 5 show uniform deformation in both parts of the sample. Higher strain always concentrates in the middle of the sample where the fracture occurs later. At the stage (0–4), we can see that the deformation is located in the center of the strain map  $\varepsilon_{ax}$  on the right hand where a wedge is glued outside the jacket. This location is clearer on the  $\varepsilon_{ax}$  map at the stage (0–5). A horizontal fracture forms completely at stage (0–6). The fracture causes the reduction of the deformation in the surrounding areas, which shows that there was release of the elastic energy stored in the material during the fracture. The fracture presents a surface with plumoses which indicates that the fracture starts on the right and then propagates to the left. This initiation point coincides with the position of the wedge.

The axial stress at rupture  $\sigma_{ax}^{pk} = \sigma_3^{pk}$  is almost similar in both experimental cases: with or without wedge (Table 1). The wedge therefore does not affect the breaking strength of the material. However, it does create a horizontal fracture and guide the fracture initiation point. Applying the DIC technique allows to track the evolution of the deformation in the material. A concentration of strain prior to fracture formation can be detected.

## 6 Conclusions

The reported results on GRAM1 show a continuous transition from extensive fracture to shear fracture with increasing confining pressure. The horizontal fractures (opening mode) form at low confining pressure. While at high pressure, shear fractures occur with an increase in fracture angle  $\Psi$  as a function of  $P_c$  under a negative to positive stress state. In addition, the morphology of fracture surfaces shows a strong correlation to confining pressure. The results herein provide the laboratory evidence for the existence of hybrid fractures which forms under the mixed tensile-compression stress. The surface morphology of the hybrid fracture is compatible with the experimental results obtained by Ramsey and Chester testing on Carra marbles (Ramsey and Chester 2004), Bobich testing on Berea sandstone (Bobich 2005) as well as in the natural fractures classified as hybrids (Ferrill et al. 2012; Engelder 1999; Reches and Lockner 1994).

The evolution of the deformation in the material during loading can be observed thanks to the DIC technique. A concentration of the deformation before the

formation of the fracture can be detected. A release of the elastic energy is also observed as soon as the fracture forms. However, the detection of the initiation and propagation of the dilatancy band is not possible in our study due to the limitation in resolution and sampling frequency of our camera. The 2D DIC technique also remains the limitations in studying 3D objects. The data approach at the level of experiments provide the evidence for the existence of hybrid fractures. Further study and 3D DIC analysis application are needed to clearly understand the specific processes that govern the hybrid fracture formation.

**Acknowledgements** We would like to thank Chemenda A.I. and P. Vacher for discussions related to this paper, J. Ambre for assistance in the laboratory. This work was supported by the Côte d'Azur Observatory, the Region Provence Alpes Côte d'Azur and GeoFrac-Net Consortium.

## References

- Bermudo Gamboa C, Martín-Béjar S, Trujillo Vilches FJ, Castillo López G, Sevilla Hurtado L (2019) 2D–3D digital image correlation comparative analysis for indentation process. *Materials* 12(24):4156. <https://doi.org/10.3390/ma12244156>
- Bertelsen IMG et al (2019) Quantification of plastic shrinkage cracking in mortars using digital image correlation. *Cem Concr Res* 123:105761. <https://doi.org/10.1016/j.cemconres.2019.05.006>
- Bésuelle P, Lanatà P (2016) A new true triaxial cell for field measurements on rock specimens and its use in the characterization of strain localization on a vosges sandstone during a plane strain compression test. *Geotech Test J* 39(5):879–890
- Bésuelle P, Desrues J, Raynaud S (2000) Experimental characterisation of the localisation phenomenon inside a Vosges sandstone in a triaxial cell. *Int J Rock Mech Min Sci* 37(8):1223–1237
- Bobich JK (2005) Experimental analysis of the extension to shear fracture transition in Berea sandstone. MS thesis, Texas A&M University
- Brace WF (1960) An extension of the Griffith theory of fracture to rocks. *J Geophys Res* 65(10):3477–3480
- Brace WF (1964) Brittle fracture of rocks. In: Judd WR (ed) *State of stress in the Earth's crust*. Elsevier, New York, pp 111–174
- Chen Y, Wei J, Huang H, Jin W, Yu Q (2018) Application of 3D-DIC to characterize the effect of aggregate size and volume on non-uniform shrinkage strain distribution in concrete. *Cem Concr Compos* 86:178–189
- Dautriat J, Bornert M, Gland N, Dimanov A, Raphanel J (2011) Localized deformation induced by heterogeneities in porous carbonate analysed by multi-scale digital image correlation. *Tectonophysics* 503(1–2):100–116. <https://doi.org/10.1016/j.tecto.2010.09.025>



- Engelder T (1999) Transitional-tensile fracture propagation: a status report. *J Struct Geol* 21(8–9):1049–1055. [https://doi.org/10.1016/S0191-8141\(99\)00023-1](https://doi.org/10.1016/S0191-8141(99)00023-1)
- Ferrill DA, McGinnis RN, Morris AP, Smart KJ (2012) Hybrid failure: field evidence and influence on fault refraction. *J Struct Geol* 42:140–150. <https://doi.org/10.1016/j.jsg.2012.05.012>
- Handin J (1969) On the Coulomb–Mohr failure criterion. *J Geophys Res* 74(22):5343–5348. <https://doi.org/10.1029/JB074i022p05343>
- Heard HC (1960) Transition from brittle fracture to ductile flow in Solenhofen limestone as a function of temperature, confining pressure, and interstitial fluid pressure. In: Griggs J, Handin JE (eds) *Rock deformation*, vol 79. Geological Society of America, Boulder, Memoir, pp 193–226
- Hoek E (1964) Fracture of anisotropic rock. *J S Afr Inst Min Metall* 64(10):501–518
- Jaeger JC, Cook NGW (1979) *Fundamentals of rock mechanics*. Chapman and Hall, London
- Lin Q et al (2019) Unifying acoustic emission and digital imaging observations of quasi-brittle fracture. *Theor Appl Fract Mech* 103:102301. <https://doi.org/10.1016/j.tafmec.2019.102301>
- Mas D, Chemenda AI (2014) Dilatancy factor constrained from the experimental data for rocks and rock-type material. *Int J Rock Mech Min Sci* 67:136–144. <https://doi.org/10.1016/j.ijrmms.2013.12.014>
- Mas D, Chemenda AI (2015) An experimentally constrained constitutive model for geomaterials with simple friction–dilatancy relation in brittle to ductile domains. *Int J Rock Mech Min Sci* 77:257–264
- Millar PJ, Murray DR (1988) Triaxial testing of weak rocks including the use of triaxial extension tests. In: *Advanced triaxial testing of soil and rock*. ASTM International, West Conshohocken
- Molina-Viedma AJ, Felipe-Sesé L, López-Alba E, Díaz F (2018) High frequency mode shapes characterisation using Digital Image Correlation and phase-based motion magnification. *Mech Syst Signal Process* 102:245–261
- Nguyen SH (2009) Étude expérimentale de la fracturation et du comportement constitutif d'un matériau frictionnel et dilatat analogue de roche réservoir. Doctoral dissertation, Nice
- Nguyen SH, Chemenda AI, Ambre J (2011) Influence of the loading conditions on the mechanical response of granular materials as constrained from experimental tests on synthetic rock analogue material. *Int J Rock Mech Min Sci* 48(1):103–115
- Nguyen VT, Kwon SJ, Kwon OH, Kim YS (2017) Mechanical properties identification of sheet metals by 2D-digital image correlation method. *Procedia Eng* 184:381–389. <https://doi.org/10.1016/j.proeng.2017.04.108>
- Pan B, Qian K, Xie H, Asundi A (2009) Two-dimensional digital image correlation for in-plane displacement and strain measurement: a review. *Meas Sci Technol* 20(6):062001
- Paterson MS, Wong TF (2005) *Experimental rock deformation—the brittle field*. Springer, Berlin. <https://doi.org/10.1007/b137431>
- Perras MA, Diederichs MS (2014) A review of the tensile strength of rock: concepts and testing. *Geotech Geol Eng* 32:525–546. <https://doi.org/10.1007/s10706-014-9732-0>
- Ramsey JM, Chester FM (2004) Hybrid fracture and the transition from extension fracture to shear fracture. *Nature* 428(6978):63–66
- Reches ZE, Lockner DA (1994) Nucleation and growth of faults in brittle rocks. *J Geophys Res Solid Earth* 99(B9):18159–18173
- Tran TPH, Bouissou S, Chemenda A et al (2019) Initiation and evolution of a network of deformation bands in a rock analogue material at brittle–ductile transition. *Rock Mech Rock Eng* 52:737–752. <https://doi.org/10.1007/s00603-018-1641-8>
- Vacher P, Dumoulin S, Morestin F, Mguil-Touchal S (1999) Bidi-mensional strain measurement using digital images. *Proc Inst Mech Eng Part C J Mech Eng Sci* 213:811–817
- Viggiani G, Hall S (2008) Full-field measurements, a new tool for laboratory experimental geomechanics. In: *4th Symposium on deformation characteristics of geomaterials*, Atlanta, vol 1, pp 3–26

**Publisher's Note** Springer Nature remains neutral with regard to jurisdictional claims in published maps and institutional affiliations.

Springer Nature or its licensor (e.g. a society or other partner) holds exclusive rights to this article under a publishing agreement with the author(s) or other rightsholder(s); author self-archiving of the accepted manuscript version of this article is solely governed by the terms of such publishing agreement and applicable law.